International Journal of Hydrogen Energy 87 (2024) 332–343

Contents lists available at ScienceDirect

International Journal of Hydrogen Energy

journal homepage: www.elsevier.com/locate/he

Particle-resolved computational modeling of hydrogen-based direct reduction of iron ore pellets in a fixed bed. Part I: Methodology and validation

Mohammed Liaket Ali *, Quentin Fradet, Uwe Riedel

German Aerospace Center (DLR), Institute of Low-Carbon Industrial Processes, Äußere Oybiner Straße 14/16, 02763, Zittau, Germany

ARTICLE INFO

Keywords:
Fixed bed
CFD
Iron oxide pellet
Hydrogen
Direct reduction process

ABSTRACT

In the pursuit of more sustainable steelmaking, stakeholders are engaging in a transformative exploration of hydrogen-based direct reduction as an alternative to conventional blast furnaces. As a bridging step between single iron ore pellets and industrial shaft furnaces, direct reduction modeling in a fixed bed configuration can play a central role for subsequent process optimization. However, this task involves numerous challenging steps: generation of a realistic packed bed structure along with a good quality mesh and, foremost, reliable transport and kinetic processes for the individual pellets. Therefore, the present work formulates a sound methodology to progress from single particle considerations to 3D-CFD simulations of iron ore reduction using hydrogen in fixed beds, further supported by validations regarding the bed structure and the overall reduction against experimental data from the literature of a 500 g iron ore bed. The current results offer new insights into the direct reduction process, revealing, for instance, the non-uniform reduction of pellets within the bed, the presence of gas pockets, or the importance of the temperature deviation due to the endothermic reduction of iron oxides with hydrogen.

1. Introduction

The iron and steel industry, crucial to modern infrastructure, faces increasing challenges due to environmental concerns as it accounts for approximatively 7% of the global anthropogenic CO_2 emissions [1]. In 2022, the integrated blast furnace/basic oxygen furnace (BF/BOF) method accounted for 71.5% of the global crude steel production [2], with associated emissions of about 1.6–2.0 t_{CO2}/t_{steel} [3]. This integrated route is already highly optimized, and the electric arc furnace route utilizing recycled steel, despite its lower carbon footprint, cannot fully replace the primary route [4]. The global quest for reduced carbon emissions and the adoption of sustainable practices has prompted a significant paradigm shift from conventional BF/BOF techniques to more environmentally friendly alternatives. Among all, the direct reduction (DR) process stands out as the highly favorable route. This transition aligns with the pursuit of eco-conscious practices as green hydrogen can be utilized.

In the steel industry, the production of direct reduced iron has been predominantly led by the MIDREX and ENERGIRON (former HYL) processes [5] over the past three decades. These processes employ a vertical shaft-type reactor to reduce iron ore pellets into metallic iron using reducing gases. However, modeling such a reactor for direct reduction presents challenges [6], and conducting industrial reactor experiments for scaling-up and process optimization can be impractical and costly. The shaft furnace modeling developed in the literature are mostly one dimensional and continuum-based [7–11]. These models do not consider complex geometry. However, Hamadeh et al. [12] developed a 2-dimensional steady-state computational fluid dynamics (CFD) model called REDUCTOR to model the DR shaft furnace, where $CO–H_2–CH_4$ as reducing gas can be used and accounting for reduction, transition and cooling sections. Such a CFD model of shaft furnace reactor can provide detailed insights and optimization capabilities but requires significant computational resources and thorough model validation. One step back from such types of large-scale reactor modeling can be laboratory-scale fixed bed modeling. In the literature very few works have been reported on the modeling of iron ore direct reduction process in fixed bed systems [13–15]. Most of these models are simplistic, meaning that they are not multi-dimensional. An accurate and detailed fixed-bed model involves multiple scales, ranging from molecular kinetics to pellet-scale diffusion and chemical reactions, and finally to reactor-scale fluid flow, heat, and mass transfer. Transitioning to hydrogen [16] represents a significant opportunity in this context.

* Corresponding author.
E-mail address: mohammed.ali@dlr.de (M.L. Ali).

https://doi.org/10.1016/j.ijhydene.2024.09.028
Received 31 May 2024; Received in revised form 16 July 2024; Accepted 2 September 2024
Available online 8 September 2024

Additionally, it underscores the importance of revisiting laboratory-scale modeling. While insights acquired from single-pellet reduction studies offer a foundational understanding regarding molecular kinetics, diffusion of reactant and product gases, chemical reaction mechanisms, etc., a significant gap remains when transitioning to the complexities of a large number of pellets in industrial-scale shaft furnaces [17,18]. Accurately simulating the aforementioned complexities within fixed bed structures has the potential to partially close these knowledge gaps [19]. It is the objective of this work to conduct and validate the modeling of the reduction of an iron ore pellet fixed bed in a 3D computational fluid dynamics environment.

The reliability and performance of a reactor model hinge on the degree of detail in the transport and kinetic models for a single pellet [20]. Many mathematical models have been developed by the researchers to predict the reaction rate; for example, Valipour et al. [21] developed a transient isothermal porous iron ore pellet reduction model using different reducing gases. Kazemi et al. [22] developed a model that combines the CFD approach for flow and mass transfer in the gas phase with the diffusion model for the solid phase. Ghadi et al. [23] compared grain model and shrinking core model for wüstite pellet reduction. The reduction process is typically a heterogeneous chemical reaction, initially controlled by the underlying chemical kinetics, but gradually shifts to diffusion-controlled or mixed regimes, especially within the optimal direct reduction temperature range of 1073 K–1323 K [24,25]. The coupled nature of transport and chemical reaction processes makes it challenging to discern their respective contributions to the overall reduction process [26]. An essential parameter that has significant impact on the kinetics of iron oxide pellet reduction is the gas film resistance, which is often overlooked by modelers. Valipour et al. [21] show how a model that doesn't consider gas film resistance fails to predict experimental data systematically. A clear understanding of the individual contributions of transport and chemical reaction processes is crucial for developing accurate models.

For scaling up, the successful transfer of parameters from a single-pellet model to a fixed-bed or reactor model is crucial. Spreitzer et al. [27] report in their review paper that the values for apparent activation energy vary widely, ranging from 11 to 246 kJ mol^{-1}, for the same reactions. A major challenge is that even the models documented in the literature cannot quantitatively model a fixed-bed reactor when independently determined kinetics and transport parameters are used. This is due to the use of effective parameters and simplified models that, to some degree, compensate for the confined wall effects on the gaseous conversion of iron ore pellets [28]. It is also evident from the literature that such simplified approaches for fixed-bed modeling utilizing literature kinetic and transport data exhibit significant deviations from the experimental data [14].

Three main approaches are possible to model a fixed-bed reactor in a multi-dimensional environment, which are phase-averaged CFD, coupled CFD-DEM, and particle-resolved CFD. The use of traditional porous media (i.e., phase-averaged) models for fixed beds offers a simplified and computationally efficient representation of the system. These models average the properties of the phases, providing a macroscopic view of the fluid and solid interactions within the bed. However, as Juritz et al. [29] report they often fail to capture the detailed particle-level interactions and the complex fluid dynamics that are characteristic of particle-packed systems. This simplification can lead to inaccuracies in predicting flow distribution, pressure drop, and mass and heat transfer, as it overlooks the heterogeneous nature of the packed bed and the local variations in these processes. The second approach, i.e. CFD-DEM, has been successfully applied for various iron ore reduction cases [30–32], ranging from fluidized-bed systems to a blast furnace. The discrete element method is utilized for the solid phase and the computational fluid dynamics is used for the fluid phase, while a coupling method combine both. This CFD-DEM approach is also called unresolved approached [33], as the grid size used for CFD is much larger than the particles. Thus, the flow around the particles is not fully resolved. As the previous approaches neglect the micro-flow structure, the so-called particle-resolved approach has been followed in the present study. This term refers to a computational fluid dynamics approach where the grid size used in the CFD simulation is much smaller than the solid particles being modelled. This allows for the detailed resolution of fluid flow around and between individual particles, providing a high-fidelity representation of the interactions between the fluid and the pellets. While the unresolved approaches rely on empirical correlations to model the heat and mass transfers, those are fully resolved in the present case. In the case of fixed-bed, it allows to more accurately capture the local flow effects that significantly impact fluid dynamics, heat, and mass transfer, especially for tube-to-particle diameter ratios $\lambda = (D/d_p)$ between 4 and 7 [34]. When it comes to the question of a particle-resolved three-dimensional CFD model for the gaseous reduction of iron ore pellet reduction process in fixed-bed, to the best of the authors' knowledge, no such work has been reported so far in the literature.

The CFD-DEM approach, in the case of iron ore reduction, is typically coupled to a shrinking core model (SCM). The model relies on a non-dimensional source term, which is well suited for the lagrangian depiction of the DEM approach. But it has inherent several flaws, as it assumes an unreacted nonporous region and a fully converted region separated by a moving reacting front, which is not an accurate representation of the reduction of single hematite pellets. In our present particle-resolved approach, the SCM cannot be simply integrated because the particles are discretized in a large number of cells. We previously developed a 1D porous solid model [35], which discretize pellets along the radius assuming a spherical symmetry. The model describes the evolution of solid and gas species, as well as changes in pellet porosity during the reduction process, as recently evidenced [36,37]. It has been furthermore shown [35] that the very same reduction behavior can be obtained in a CFD environment when the pellet boundary information from the CFD is accounted for in the 1D model. Thus, the 3D particle-resolved approach used in this study utilizes reduction kinetic data derived from the aforementioned 1D porous solid model.

Constructing fixed-bed structures using traditional experimental techniques, such as scanning electron microscope (SEM) imaging [38], micro-computed tomography (micro-CT) [39,40], or magnetic resonance imaging (MRI) [38], provides high-resolution data and detailed structural information. However, these methods have notable drawbacks, including being time-consuming, costly, and requiring specialized equipment and expertise. These limitations make them less practical for routine use, especially in industrial settings where rapid and cost-effective modeling approaches are needed. This study utilizes the discrete element method (DEM) [41] to generate a fixed bed of spherical pellets, emphasizing its physical nature instead of using statistical methods [29]. De Klerk et al. [34] report that statistical methods like the Monte-Carlo-based method generate a less dense bed and much more damping oscillatory behavior in the radial porosity distribution. The DEM approach allows for a detailed and realistic representation of the particle interactions and spatial arrangement within the bed, capturing the mechanical and dynamic behaviors of individual pellets. This method is advantageous because it accurately reflects the physical processes governing the formation and behavior of the fixed bed. Unlike statistical methods, which may oversimplify the system and overlook critical particle-level phenomena, DEM offers a robust and precise modeling technique that enhances the understanding and prediction of reactor performance. A finite element mesh generator (Gmsh) [42] is then used to create an appropriate 3D mesh based on the positions and sizes of the pellets from the DEM simulation, resolving skewed cells in narrow contact regions among pellets through appropriate treatments and refinements.

This article is the first in a two-part series. The second part examines the influence of particle shape, comparing spherical pellets with non-

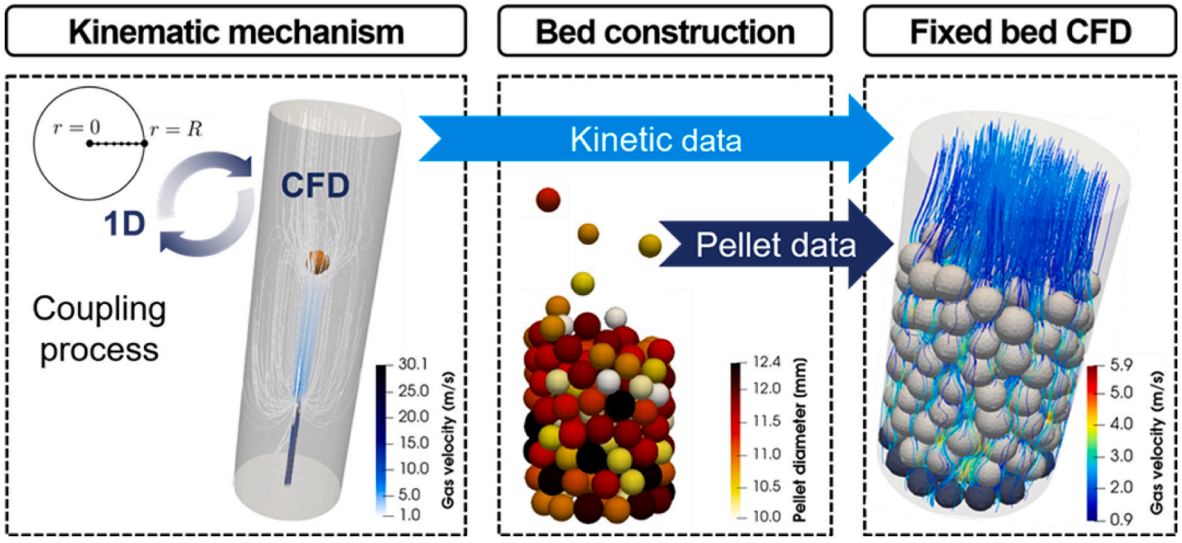

Fig. 1. General workflow of CFD modeling for fixed bed iron ore direct reduction.

spherical particles [43]. This first part is composed of two main sections – method description followed by results and discussions – both sections being sub-divided into three steps as presented in the general workflow in Fig. 1 and detailed below.

1. Developing a transient 3D-CFD model to simulate the H_2-based iron oxide pellet reduction process utilizing the kinetic and transport data of a previously developed 1D model [35,44].
2. Generating a random fixed bed of 0.5 kg iron ore pellets using DEM simulation.
3. Performing CFD simulations of iron oxide pellet reduction process using H_2 as a reducing gas in a fixed bed, considering available experimental data [14] for model validation.

2. Methods

2.1. Kinetic mechanism development from the reduction of single pellets

In this work, we use our previously developed 1D porous solid model to describe the reduction of single iron ore pellets [35]. The main governing equations are reminded here for the sake of completion. This model discretizes the pellet along the radius assuming spherical symmetry. Due to this approach, the model can be smoothly adopted in a 2D or 3D environment. To get a reliable kinetic mechanism, it is necessary to validate against various experimental conditions. Our porous solid model already showed maturity in predicting single iron ore pellet reduction process using H_2 but also syngas, including complex phenomena like carbon deposition and cementite formation [44]. The governing equations considered in the 1D model are as follows, for gas species:

$$\frac{\partial \varepsilon C_i}{\partial t} = -\nabla\cdot\left(-D^{\text{eff}}\nabla C_i\right) + \dot{s}_i, \quad i \in \text{gas species}, \tag{1}$$

and for solid species:

$$\frac{\partial (1-\varepsilon)\rho_j X_j}{\partial t} = M_j \dot{s}_j, \quad j \in \text{solid species}. \tag{2}$$

These two equations are valid in the whole porous pellet domain.

In Equation (1), the gas species concentrations are driven by the diffusion and reaction terms ($\dot{s}_i$). The effective diffusivity is given by $D^{\text{eff}} = (\varepsilon/\tau)D$, where D is the molecular bulk diffusion coefficient and τ is the tortuosity factor. Considering the transport of gas through a porous medium, the porosity term, ε, is introduced in the equations. The solid species mole fraction with reaction is presented in Equation (2) where ρ_j and X_j are respectively the density of the species j in a pure solid state and the mole fraction of the species j. The governing equations have been reformulated to isolate the temporal derivatives of the gas concentration, solid mass fraction and porosity:

$$\frac{\partial C_i}{\partial t} = \frac{1}{\varepsilon}\nabla\cdot\left(D^{\text{eff}}\nabla C_i\right) + \frac{1}{\varepsilon}\dot{s}_i - \frac{C_i}{\varepsilon}\frac{\partial \varepsilon}{\partial t}, \quad i \in \text{gas species}, \tag{3}$$

$$\frac{\partial X_j}{\partial t} = \frac{1}{1-\varepsilon}\frac{M_j}{\rho_j}\dot{s}_j + \frac{X_j}{1-\varepsilon}\frac{\partial \varepsilon}{\partial t}, \quad j \in \text{solid species}. \tag{4}$$

$$\frac{\partial \varepsilon}{\partial t} = -\sum_j \frac{M_j}{\rho_j}\dot{s}_j, \quad j \in \text{solid species}. \tag{5}$$

The details of the derivation and subsequent discretization and solving are given in our previous publication [35].

The coupling of the 1D model with a 3D-CFD environment is beneficial for improving the accuracy of simulations as the 1D model assumes a constant boundary condition or relies on a mass transfer coefficient, which adds an additional unknown variable to the system of equations. Therefore, a 3D-CFD model of the entire reactor domain is employed to accurately calculate the concentration of gas-phase species on the pellet surface. The gas species concentration obtained from the 3D-CFD model serves as a boundary condition in the 1D model, allowing for iterative exchange of information until both models yield sufficient agreement. This way, the chemistry and transport data from the 1D model can be confidently used in further CFD simulations. The detailed model coupling has been discussed in our previous work [35]. The modeling framework of the 3D-CFD model will be discussed in Section 2.3. Table 1 includes the experimental conditions for the coupling process.

The gaseous reduction of iron ore undergoes the following sequence: Fe_2O_3 (hematite) → Fe_3O_4 (magnetite) → FeO (wüstite) → Fe (metallic iron). The gas-solid reduction is a complex process where all the sub-processes (external and internal transport, as well as the successive

Table 1
Experimental data [22] for a single pellet iron oxide reduction process.

Case ID	T1073P26	T1123P26	T1073P34	T1123P34
Temperature [K]	1073	1123	1073	1123
Porosity, ε [%]	26	26	34	34
Pellet composition	Fe_2O_3: 0.96, Gangue: 0.04			
Pellet diameter, d [mm]	11			
Flow rate, Q [Nl/min]	2			

reactions) can control the global rate. The reaction rate is dominated initially by the chemical reaction and competing with the internal gas diffusion simultaneously. And at the end of the reduction process, the reaction rate is dominated by internal diffusion [24]. There is a general claim that when the gas flow rate exceeds 1 Nl/min, external mass transfer is not a rate-limiting factor anymore in the case of single pellets. However, contrary to the claim, Kazemi et al. [45] experimentally demonstrate that the gas flow rate at 1.5 and 2 Nl/min has an impact on the pellet reduction. The current 1D model considers this flow rate effect by providing the accurate reducing gas boundary condition from the CFD simulations.

The overall chemistry with pure hydrogen can be described [44] with the following stages:

$$3\ Fe_2O_{3(s)} + H_{2(g)} \rightarrow 2\ Fe_3O_{4(s)} + H_2O_{(g)}$$

$$Fe_3O_{4(s)} + H_{2(g)} \rightarrow 3\ FeO_{(s)} + H_2O_{(g)}$$

$$FeO_{(s)} + H_{2(g)} \rightarrow Fe_{(s)} + H_2O_{(g)}$$

The three reactions in this study are deemed irreversible for the sake of simplification. Furthermore, separating the reverse reaction rates from the forward rates is almost impossible based on the current experimental data available.

2.2. Numerical construction of a fixed bed with DEM simulation

The basic strategy of the particle-resolved fixed bed generation used in this work is as follows.

1. A random fixed bed is generated using the discrete element method with spherical particles accounting for 0.5 kg iron ore pellets
2. A calculation domain is created based on the particle position and equivalent diameter from the first step
3. An optimized mesh is produced for the calculation domain, including the pellets and the voids in between

The discrete element method is an explicit numerical method used for modelling movements and interactions of particles, including collisions with walls. In OpenFOAM [46], a soft-sphere based approach is employed for DEM simulations. The "icoUncoupledKinematicParcelFoam" solver has been used to solve the interaction between iron ore particles and reactor walls. In this approach, each of the particles is treated as a deformable body capable of undergoing multiple, simultaneous collisions. The main test case setups include.

a. Choose correct physical constant properties for iron ore pellet/reactor wall
b. Include necessary sub models, like "particle forces", "injection models" and "pair collision models (pellet-pellet and pellet-wall)" and set the right coefficients for all these models.
c. Adjust the injection model to accommodate the experimental pellet size distribution

Newton's law of motion is applied to each particle, considering particle-particle and particle-wall interactions, as well as gravitational force. The drag force from the gas phase (continuum phase) is neglected, resulting in the momentum conservation equation.

$$m_i \frac{d\mathbf{v}_i}{dt} = \mathbf{F}_g + \mathbf{F}_c. \tag{6}$$

In the left part of the equation, m_i is the mass of the particle i and $\frac{d\mathbf{v}_i}{dt}$ represents changes in the i^{th} particle velocity over time t. On the right-hand side of equation (6), $\mathbf{F}_g$ and $\mathbf{F}_c$ represent the gravitational force acting on the particles and the contact forces, respectively. $\mathbf{F}_c$ is the sum of the particle-particle and particle-wall interaction forces,

$$\mathbf{F}_c = \sum_{particle-particle} \mathbf{F}_c + \sum_{particle-wall} \mathbf{F}_c. \tag{7}$$

These contact forces are calculated using a spring-dashpot model as portrait in Fig. 2. When the particles collide with each other or with the wall, they are pushed away. This elastic property of the collision is considered by the "spring" part of the model. But the collision also includes dissipation of energy by reducing the collision forces. The "dashpot" part of the system represents this energy dissipation. This contact force has normal and tangential components. Now considering the unit normal vector, **n** and tangential vector, **t**, the contact force can be written as,

$$\mathbf{F}_c = F_N\mathbf{n} + F_T\mathbf{t}, \tag{8}$$

where, F_N and F_T represent the magnitude of the normal and the tangential force, respectively. As we see from Fig. 2, there is an overlap (δ_N) between colliding particles, which represents the deformation during the collisions.

The contact force in the normal direction is calculated using Hertzian contact theory as done by Cundall et al. [41],

$$F_N = -k_N\delta_N^{\frac{3}{2}} - \eta_N.u_N^{ij}, \tag{9}$$

where, k_N, δ_N, η_N, and u_N^{ij} represent the normal spring stiffness, deformation in the normal direction, damping coefficient, relative velocity between colliding particles i and j in the normal direction, respectively.

The normal spring stiffness depends on the effective Young's modulus E^* and equivalent radius R.

$$k_N = \frac{4}{3}E^*\cdot\sqrt{R}. \tag{10}$$

The damping coefficient is calculated as Tsuji et al. [47].

$$\eta_N = \alpha\sqrt{M_{eq}k_N}\cdot\sqrt[4]{|\delta_N|}, \tag{11}$$

where α is an empirical coefficient related to the restitution coefficient and the equivalent particle mass, M_{eq}, is a function of the mass of particles i and j, M_i and M_j.

The tangential force F_T in equation (8) is calculated like the normal

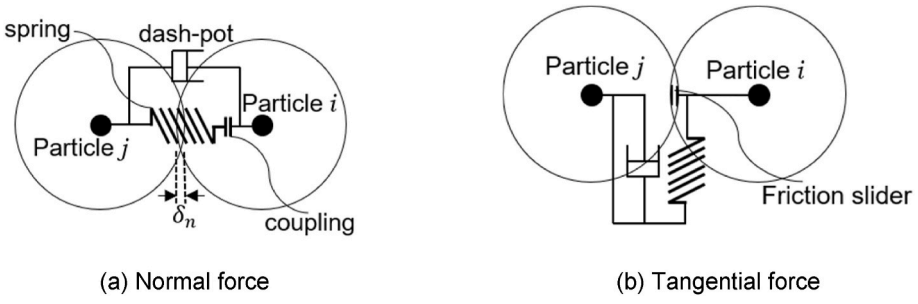

Fig. 2. Soft sphere approach in DEM; (a) Spring slider dashpot system for normal collision, (b) Spring slider dashpot system for tangential collision.

force F_N if the tangential force is smaller than the sliding friction force ($|k_T \cdot \delta_T| < |k_N \cdot \delta_N| \cdot \mu$, here μ is the coefficient of friction), meaning that the particles do not slip:

$$F_T = -k_T \delta_T^{\frac{3}{2}} - \eta_T u_T^{ij}. \quad (12)$$

The tangential stiffness k_T can be calculated as

$$k_T = 8.0\sqrt{R \cdot \delta_T} \cdot G^*, \quad (13)$$

where, the effective shear modulus, G^* is related to the Young's modulus.

If the tangential force is greater than the sliding friction force, which means the particles slip. Then the tangential force is calculated as such,

$$F_T = \mu F_N. \quad (14)$$

All the equations mentioned above are also valid for calculating the particle-wall collision forces by assuming the wall is a hard surface. A total of 212 particles with varying sizes are fed from a hopper positioned at the top of the reactor with an initial velocity of 4 m s^{-1} to mimics the real-world scenario and fall due to gravity. A total of 187 pellets are iron ore pellets, and a layer of 25 alumina pellets is placed at the bottom of the bed. The packing generation is considered complete when the particles reach near-zero velocity. The bed geometry and mesh generation are illustrated in Fig. 3. The contact forces for the discrete element method simulations are calculated using the spring-dashpot model, as detailed in Table 2, which outlines the numerical parameters considered for the modelling.

The size distribution of the pellets between 10 and 12.5 mm in diameter is considered based on the experimental case [14] to be reproduced. As the bed generation of DEM simulation is finished, the post-processing stage involves extracting the centers of each pellet and their respective diameters. A mesh generator called "Gmsh" [42] is used to generate the 3D bed mesh. Fig. 4 illustrates the contact point treatment method with the global shrinking technique that has been applied to every pellet and the mesh structure of the fixed bed. The mesh itself is a single entity, but mesh parts corresponding to the solid and gas phase are shown separately in Fig. 4 (b) for visualization purposes. The mesh is unstructured and the pellet surfaces have been meshed in 2D, prior to volume meshing, in order to respect their spherical geometry. The final mesh counts 287,000 cells. A major challenge while generating a fixed bed mesh is the local refinement at the contact points between the adjacent pellets and between the pellets and the wall. Local refinements will result in meshes with highly skewed cells or with a large number of cells. There are several techniques to tackle this issue. Shrinking the pellets globally by a small percentage (0.5–1%) is a commonly accepted practice [48,49]. Using this technique eliminates the contact points, allowing the mesh generator to have adequate space to create good-quality cells. In general, this technique has some drawbacks, including errors in the void fractions within the bed and the pressure drop in the bed due to the formation of artificial gaps. But for a small bed height of approximately 90 mm, like in our cases, the pressure drop can be negligible.

2.3. Reactive CFD modelling of a fixed bed

Based on the physical mesh, a reactive CFD simulation for a fixed bed was conducted in a modified solver in OpenFOAM [46]. The DEM simulation data is additionally used to set porous zones within the bed. The CFD model solves for gas velocity, gas concentration, gas transport in the solid phase, and the transient evolution of solid species. The model also accounts for variations in pellet porosity and gas-solid chemistry. The governing equations for the gas phase include continuity, momentum, and species balance equations (15)-(17), while the solid species and the porosity evolution equations are described by equations (18) and (19), respectively. This set of governing equations applies to the entire domain of the reactor, including the pellets:

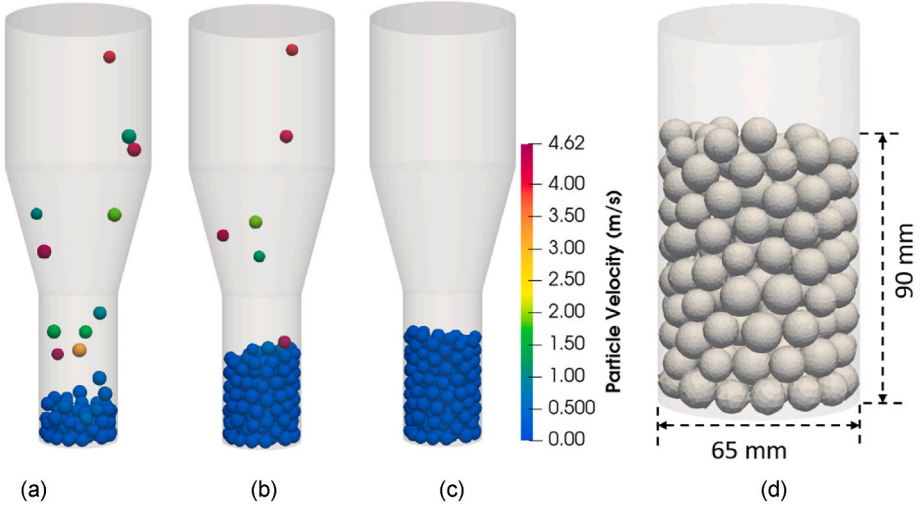

Fig. 3. Illustration of particle-resolved CFD approach for packed bed generation. (a), (b), and (c) show generating the pack by using DEM simulations, (d) creating bed geometry using the input from the DEM simulations when all the particles are settled.

Table 2
Numerical parameters used in DEM simulations.

Parameters	Value	Unit	Parameters	Value	Unit
Reactor diameter	65	mm	Number of particles	212	–
Reactor length	120	mm	Particle density, ρ_p	5300	kg m^{-3}
Feeder diameter	120	mm	Poisson's ratio, ν	0.35	–
Feeder length	103	mm	Youngs's modulus, E	1.8×10^8	Pa
Particle diameter, d	10.0–12.5 mm	mm	Coeff. restitution, α	0.9	–
Initial particle velocity	4	m s^{-1}	Coeff. friction, μ	0.1	–

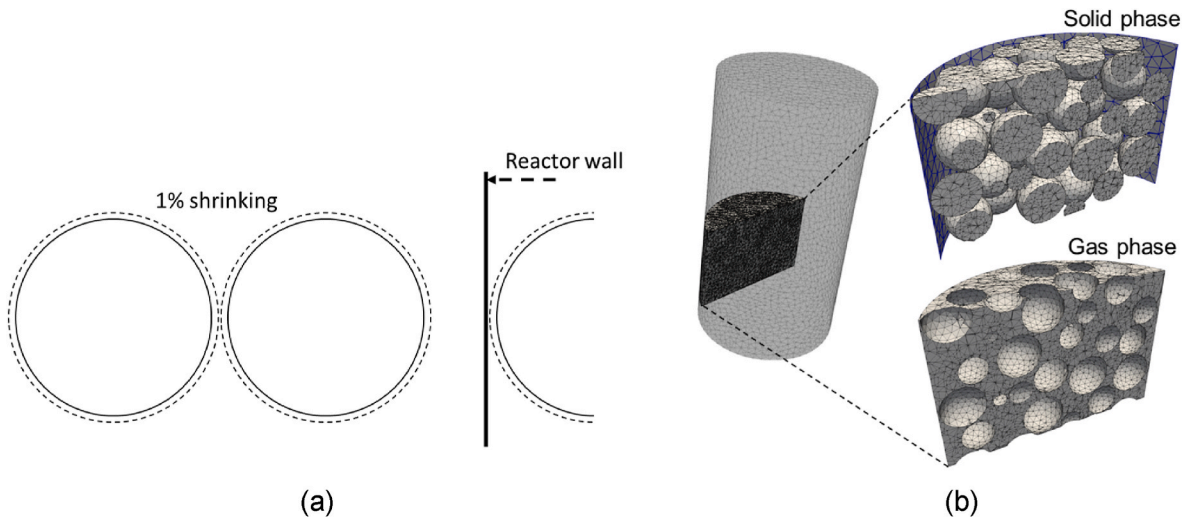

Fig. 4. (a) Global shrinking method for contact point treatment, (b) Mesh structures of the iron ore fixed bed for gas and solid phases. An exemplary mesh portion has been chosen for better visualization.

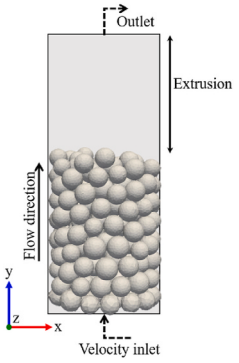

Fig. 5. Schematic overview of the iron ore pellet packing model and boundary conditions used for the CFD simulations.

$$\frac{\partial \alpha_g \rho_g}{\partial t} + \nabla \cdot \left(\rho_g \mathbf{v}_g\right) = S_g, \tag{15}$$

$$\frac{\partial \alpha_g \rho_g \mathbf{v}_g}{\partial t} + \nabla \cdot \left(\rho_g \mathbf{v}_g \mathbf{v}_g\right) = \nabla \cdot \bar{\bar{\tau}} - \nabla p + \rho_g \mathbf{g} + \mathbf{M}_{sg}, \tag{16}$$

$$\frac{\partial \alpha_g \rho_g Y_{g,i}}{\partial t} + \nabla \cdot \left(\rho_g Y_{g,i} \mathrm{v}_i\right) = -\nabla \cdot \mathbf{j}_{g,i}^{\mathrm{eff}} + M_i \dot{\omega}_i + M_i s_i \quad i \, \epsilon \text{ gas species}, \tag{17}$$

$$\frac{\partial X_j}{\partial t} = \frac{1}{(1-\varepsilon)} \frac{M_j}{\rho_j} \dot{s}_j + \frac{X_j}{(1-\varepsilon)} \frac{\partial \varepsilon}{\partial t} \quad j \, \epsilon \text{ solid species}, \tag{18}$$

$$\frac{\partial \varepsilon}{\partial t} = -\sum_j \frac{M_j}{\rho_j} \dot{s}_j \quad j \, \epsilon \text{ solid species}. \tag{19}$$

The Section Nomenclature defines the symbols used in the governing equations mentioned above and throughout the article. However, certain terms require additional consideration.

- In Equation (15), the net mass transfer between gas and solid phases is $S_g = \sum_i M_i \dot{s}_i = -\sum_j M_j \dot{s}_j$. Where, $\dot{s}_i$ is the chemical source term of a single chemical species.
- The momentum sink term $\mathbf{M}_{sg}$ in Equation (16) represents the flow through the porous medium. In this CFD model, the Darcy's law $\mathbf{M}_{sg} = -\mu_g \mathbf{D}\, \mathbf{v}_g$ is used, where $\mathbf{D}$ is a constant coefficient.
- In all the governing equations α_g represents the gas volume fraction or can be eventually termed as porosity. For $\alpha_g = 1$, i.e. in the gaseous phase, there is no mass transfer between the phases ($S_g = 0$). The chemical source terms and momentum also vanish ($\dot{s}_i = 0$ and $\mathbf{M}_{sg} = 0$).
- The homogeneous chemistry term is $\dot{\omega}_i$, which is zero due to the absence of homogenous chemistry in our reactive system.

More information regarding the governing equations are discussed in one of our previously published works [35].

Fig. 5 depicts the overall layout and the boundary conditions of the CFD fixed-bed model. The reactor wall has a "no-slip" boundary condition, and the reactive gas is injected from the bottom of the bed and exits at the top of the reactor. The operating conditions of the reactive CFD simulations are detailed in Table 3.

The temperature of 1173 K listed in the table is the initial temperature of the reduction. The CFD model also considers changes in bed temperature during the reduction process by using the experimental temperature profile from Beheshti et al. [14].

The primary evaluation criterion for the CFD model is the global conversion degree F, which is defined as:

$$F = \frac{m_0 - m(t)}{m_0 - m_\infty}, \tag{20}$$

where the following notation is used: m_0 initial pellet mass, $m(t)$ mass at time t, m_∞ theoretical mass after complete reduction. The values 0 and 1 for F indicate no conversion (Fe_2O_3 and Gangue) and complete conversion (Fe and Gangue), respectively.

Table 3
Key operating conditions for CFD fixed-bed modeling.

Reactor	Height = 120 mm	Radius = 32.5 mm	
Iron ore pellets	Iron ore = 187 Alumina = 25	Porosity = 27% Diameter = 10.0–12.5 mm	0.971 – Fe_2O_3 0.029 – Gangue Mass basis
Reducing gas	75% H_2, 25% N_2	Flow rate = 50 L/min	Temperature = 1173 K

3. Results and discussions

3.1. Coupling 1D and 3D-CFD models

The results of the reduction of a single pellet with the 1D and CFD model are shown with case ID T1123P26 as an example in Fig. 6 (a). The results of the 1D model match closely the experimental data as the chemical parameters are determined from curve fitting on the four considered single pellet cases. The CFD run using these kinetic parameters – iteration00 in Fig. 6 (a) – results in a slower reduction rate as the hydrogen concentration on the pellet boundary is lowered by the reduction process. The average hydrogen concentration in this first CFD iteration is given in the subplot of Fig. 6 (a). Adopting the new boundaries from the CFD simulation in the kinetic parameter determination results in a close alignment between the 1D and CFD model outcomes, with minimal discrepancies, as seen with the iteration01 curve. These small differences can be attributed to the consideration of an average H_2 concentration at the phase-boundary. As evident from Fig. 6 (b), the boundary conditions exhibit asymmetry in the downstream and upstream surface. This is due to the setup, with gas inflow from the bottom side.

The CFD velocity contour field in Fig. 7 (a) shows high gas velocity at the reactor inlet and recirculation at the rear side of the pellet, with the gas stream splitting laminarly around the pellet without any noticeable wake behind the pellet. Fig. 7 (c) and (d) illustrate that there is a higher concentration of H_2 at the upstream part of the pellet compared to the downstream part. This creates a concentration gradient across the pellet, resulting in higher diffusion in the upstream part of the pellet compared to the downstream part.

Fig. 8 depicts the spatial distribution of iron oxide phases at 300 sec. in detail, showing rapid consumption of hematite and magnetite with wüstite becoming the dominant phase by encapsulating them. Additionally, iron phase starts to appear at the surface of the pellet as shown in Fig. 8 (d).

When considering the evolution of iron oxides over time, as shown in Fig. 9 (a), there is an initial rapid conversion of hematite, resulting in a sharp peak in magnetite and a steady increase in the wüstite phase. After around 75 sec., the total magnetite amount starts to decrease while the wüstite phase continues to increase. At around 400 sec., the total wüstite amount ceases to increase as almost all hematite and magnetite are already consumed and the iron phases thrive from the surface to the center of the pellet. Finally, Fig. 9 (b) demonstrates the accuracy of both types of models in predicting experimental data with a successful coupling between them.

Table 4 lists the optimized kinetic data after coupling both the models. The reactive fixed-bed simulation will employ this kinetic information.

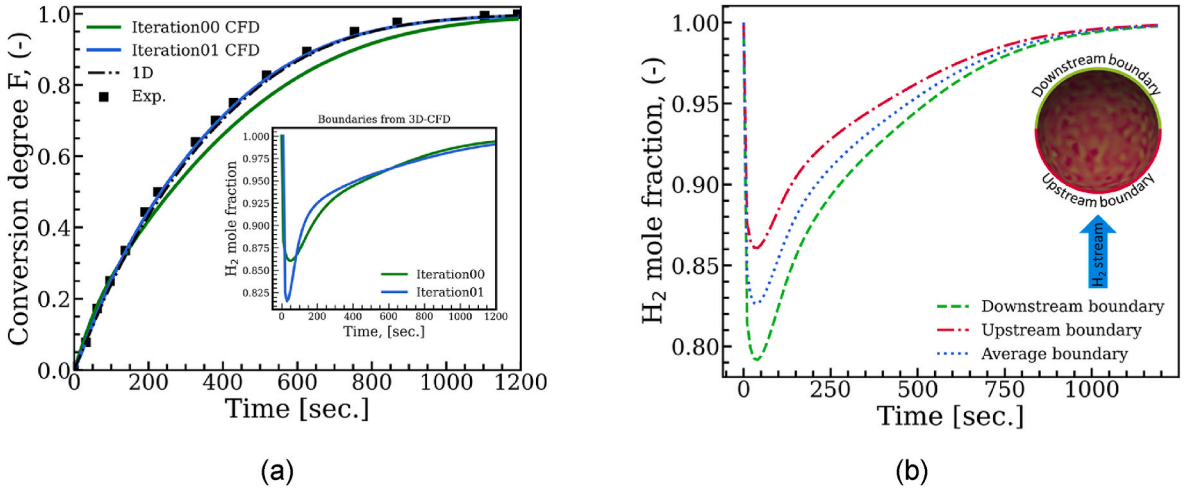

Fig. 6. (a) Iterative coupling process of 1D and 3D-CFD models with a subplot showing the H_2 concentration boundary conditions from the 3D-CFD model (Case ID T1123P26), (b) Variation of average H_2 concentration in the pellet boundary film.

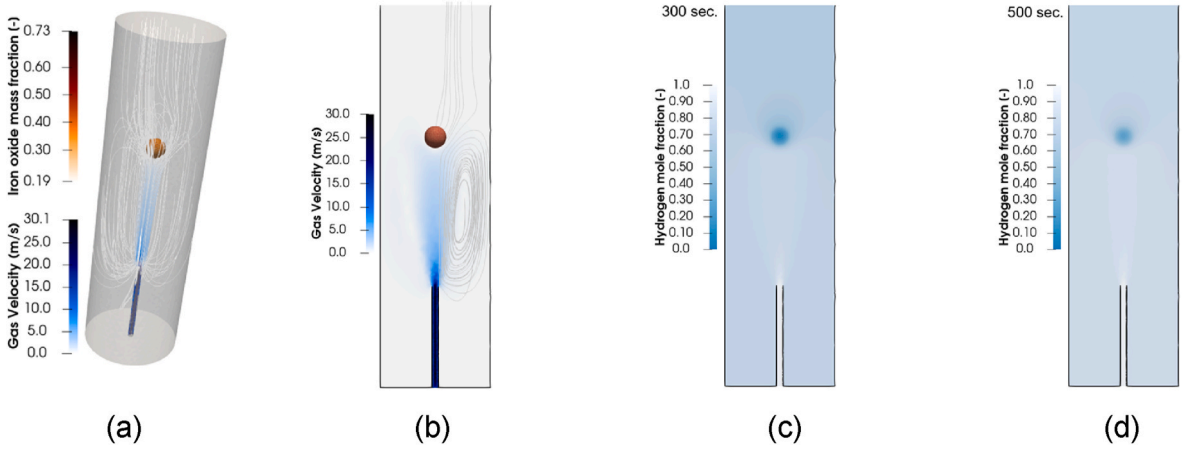

Fig. 7. Single pellet reactor flow field CFD simulations. (a) Gas velocity stream in a 3D domain, (b) velocity contour in an exemplary plane, (c) & (d) Hydrogen gas concentration at time 300 sec. and 500 sec. respectively.

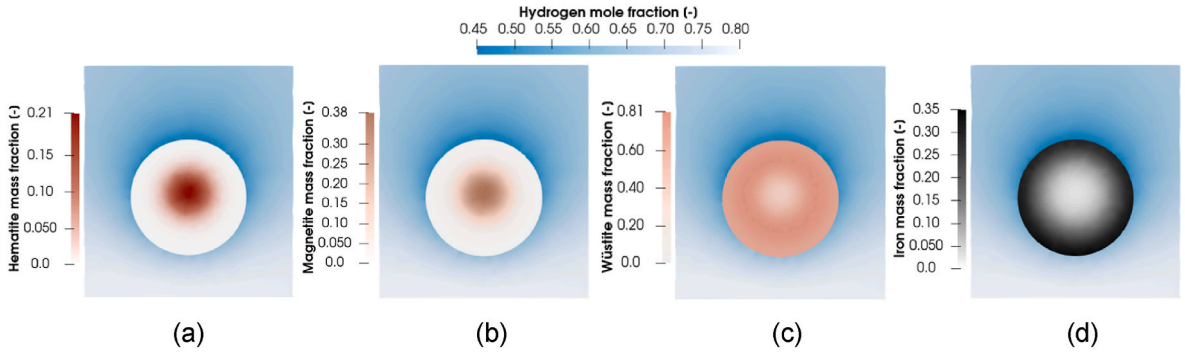

Fig. 8. Intermediate solid species distribution at 300 sec. with hydrogen concentration in the vicinity of the pellet; (a) Hematite (Fe_2O_3), (b) Magnetite (Fe_3O_4), (c) Wüstite (FeO), and (d) Reduced Iron (Fe) mass fraction.

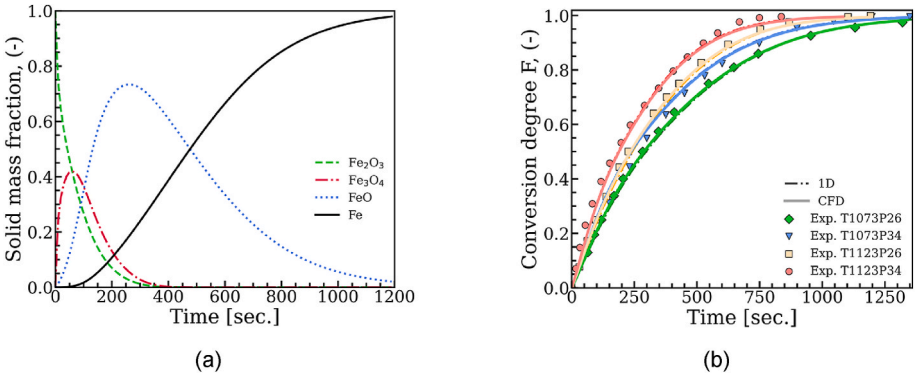

Fig. 9. (a) Solid species evolution for a 26% porous pellet at 1123 K (T1123P26), (b) Overall conversion degree vs. time. Solid line, dash-dotted line and symbols represent the CFD model, the 1D model results and experimental data, respectively.

Table 4
Surface reaction steps and the kinetic rate parameters of iron oxide reduction.

Reactions	Pre-exponential factor A [cm, mol, s]	Activation energy E_a [kJ/mol]
$3\,Fe_2O_{3(s)} + H_{2(g)} \rightarrow 2\,Fe_3O_{4(s)} + H_2O_{(g)}$	131,446	80.714
$Fe_3O_{4(s)} + H_{2(g)} \rightarrow 3\,FeO_{(s)} + H_2O_{(g)}$	391,710	80.027
$FeO_{(s)} + H_{2(g)} \rightarrow Fe_{(s)} + H_2O_{(g)}$	75,393	77.430

3.2. DEM bed characteristics and validation

The structure of a fixed-bed reactor is typically characterized by the local radial average bed porosity and bulk bed porosity. In order to gain confidence in the DEM-simulations, both of these characteristics are compared against experimental data. The local radial bed porosity is calculated as

$$\varepsilon(r) = \frac{A_{\text{solid}}}{A_{\text{total}}} = \frac{A_{\text{solid}}}{2\pi \cdot r \cdot h_{\text{plane}}} \,. \tag{21}$$

Here, around 30 concentric planes are considered for the calculation. In the above-mentioned equation, r, A_{solid} and A_{total} represent the radial

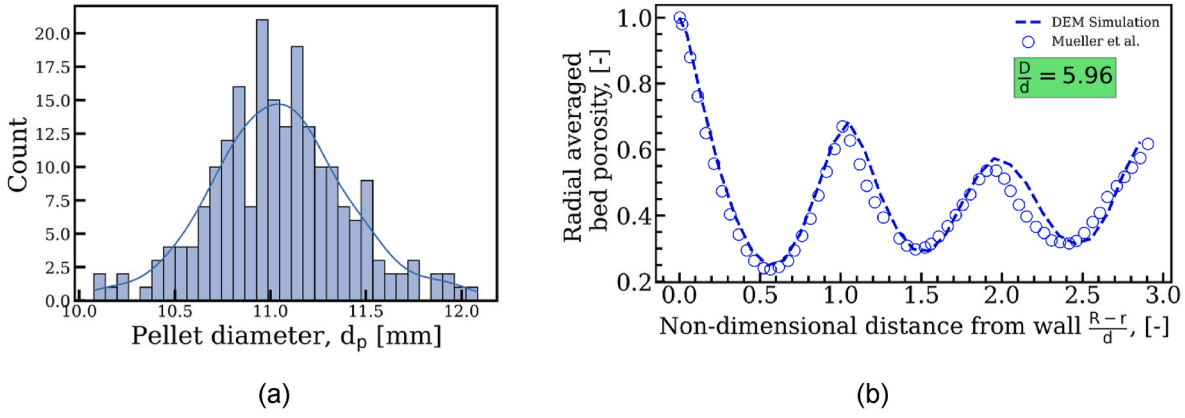

Fig. 10. (a) Pellet size distribution in packed bed, (b) Radial average bed porosity distribution; R and r represent the radius of the reactor and the pellet, respectively.

distance of the plane from the center, the area of the pellet's cross-section in that specific plane, and the total area of that specific plane, respectively. Fig. 10 (a) shows that the size of the pellets in the generated bed follows a normal distribution, with the majority of the pellets ranging from 10.7 to 11.5 mm. Additionally, Fig. 10 (b) presents the radial-averaged bed porosity plotted against the radial position within the cylinder, starting from the tube wall and normalized to the particle diameter (d). The curve looks like a damping oscillatory function, with the radial porosity at the wall being 1 and the first minimum at 0.5, followed by the first maximum at the position 1.0. The current work, with a D/d ratio of ~5.96, has been compared to Mueller et al. [50], who used a similar ratio, showing overall good agreement with their experiment data. The calculated bulk bed porosity in this work is 0.44, which is consistent with correlation values of 0.41, 0.41, and 0.42 from the literature [51–53].

3.3. Fluid dynamics and reduction behavior

The gas velocity profile of the fixed bed is shown in two exemplary planes in Fig. 11. The maximum axial velocity in the reactor is 5.6 times the superficial inlet velocity (~1 m s^{-1}) due to the channeling in the bed, which can even be exceeded by a factor of 11 according to Jurtz et al. [29]. To ensure a uniform flow field of the reducing gas, alumina pellets are placed at the bottom layer. The velocity is notably high in the narrow interstitial spaces, reaching its maximum in certain regions, while the gas exits the upper part of the bed. The areas in close proximity to the contact points, however, exhibit relatively low velocities and may even have stagnant zones. The right side of plane 1 near wall and the lower left side of plane 2 display wall effects on the gas velocity, with velocities reaching as high as ~3 m s^{-1}. Furthermore, the gas velocity gradually increases with the height of the reactor bed due to the pressure drop in the axial direction. The flow field of hydrogen at 500 sec. is shown in Fig. 12. The same flow field at other simulation times can also be seen in Fig. S1 of the supplementary materials. It is quite obvious that the H_2 concentration in the gas phase is higher at the bottom part than at the top part of the bed due to reaction progression. The concentration of water - the product from the reduction - is higher directly inside the pellets than in the gas phase showing that outward diffusion of water is a limiting process. This obviously do not apply to the inert alumina balls. To further quantify the hydrogen molar fraction inside the gas phase, three profiles over radial have been extracted and are displayed in Fig. 12 (b). The water amount can be easily deduced from the hydrogen molar fraction and the one of nitrogen, constant and equal to 0.25. At a temperature of 1173 K, the ratio of hydrogen to water plus hydrogen ($[H_2]/([H_2]+[H_2O]$), also called gas utilization degree) should be at least of 62% to be in the stability phase region of iron [54]. If the bottom layer is always in the stability region of iron, wüstite is the stable solid species in the middle and top layers over a certain period of time. This effect is even stronger as the bed height is high. The profile of each section over time is quite similar to the boundary hydrogen concentration for a single pellet as visible in Fig. 6. The concentration drops quickly and further slowly increases as the reduction rate decreases over time. The mass fraction fields of iron and its oxides at 500 sec. are shown in Fig. 13, as well as the local conversion degree. The same fields at other times can be found in the supplementary material. The plane is not cutting the pellets exactly at their centers. The large disks have been cut close through the center, while the smallest were met on the pellet periphery. So, to compare the state of different pellets, disks of similar sizes should be compared to the pellet size distribution, which causes some uncertainties. Fig. 13 (a) and (b) show presence of hematite and magnetite only in the pellet cores at 500 sec. due to the rapid transition to the wüstite phase [55]. However, the transition from wüstite to the iron phase is comparatively slower than other phase transitions, resulting in a ring-shaped wüstite phase throughout the bed, as seen in Fig. 13 (c). The presence of iron phase in the bed is consistent with the evolution of the other three phases. Pellets in the lower part of the bed exhibit in general a higher local conversion degree than pellets in the upper part and that at all times. It is a direct consequence of the hydrogen distribution within the bed, as seen previously. The difference is particularly notable at 500 and 1000 sec. At the latter stage of the process a compensation effect occurs: pellets on the bottom are close to complete reduction, making their rate of reduction very slow, slower than that of the pellets at the top.

The global conversion degree of the bed over time has been derived by integrating the local conversion degree over all pellets and the results are given in Fig. 14 along with the experimental data from Beheshti et al. [14]. The model results under isothermal conditions show a higher iron ore reduction compared to the experimental data. The endothermic reactions in the bed cause the pellet temperature to deviate from the initial temperature. Our model accounts for this by incorporating the mean experimental bed temperature evolution, as shown in the subplot of Fig. 14, which provides temporal but not spatial resolution of temperature within the fixed bed. Hence, the model does not account for local temperature variations. We anticipate that temperature gradients within the bed, with higher temperatures at the bottom layers and lower temperatures at the top due to the endothermic nature of the H_2 reduction reactions, could impact the local reaction rates. While the overall reduction degree may not be significantly affected by these gradients, they could lead to notable discrepancies in the reduction degree between the top and bottom bed layers. As we see, taking the mean temporal temperature correction into account, the model accurately predicts the experimental data, emphasizing the importance of considering the real

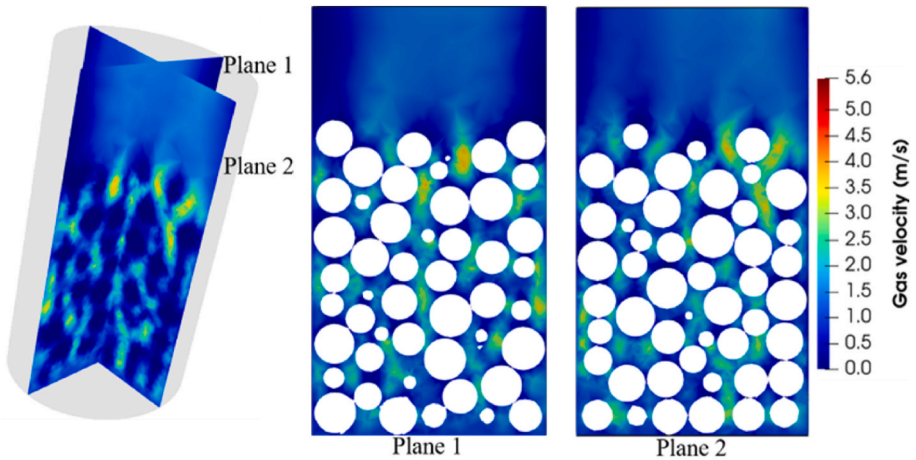

Fig. 11. Gas velocity contour planes in the fixed bed taken along the main flow direction at 500 sec.

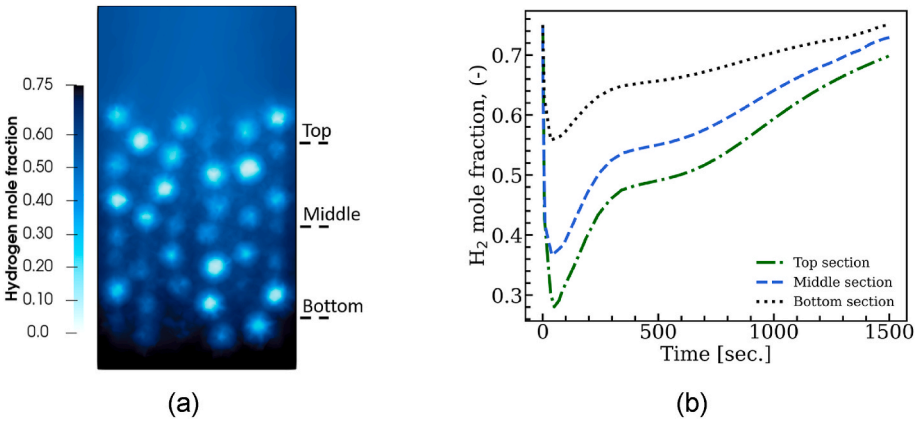

Fig. 12. (a) H_2 gas concentration plane at 500 sec. and (b) H_2 gas concentration comparison in three different bed heights.

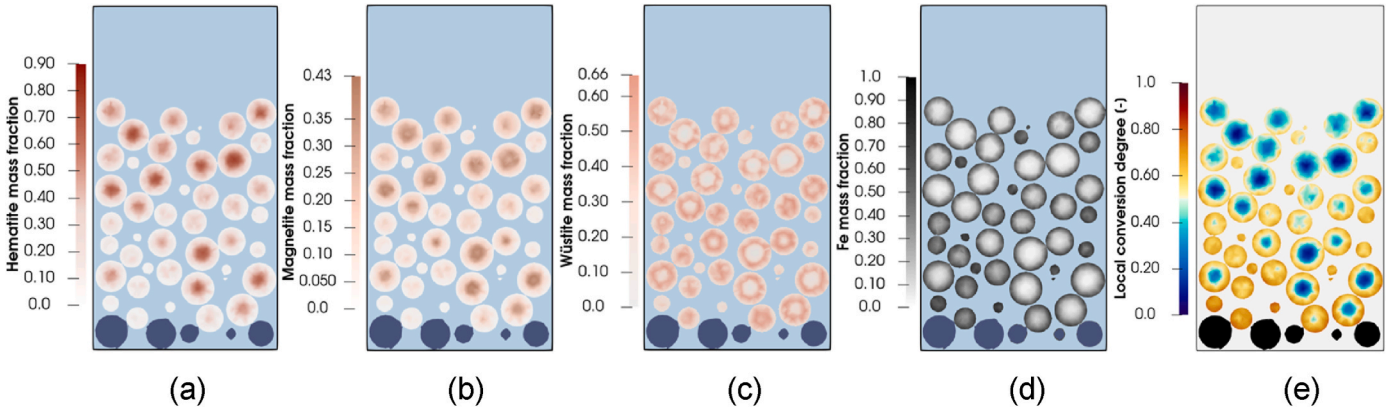

Fig. 13. Solid mass fraction planes at 500 sec. - (a) Fe_2O_3, (b) Fe_3O_4, (c) FeO, (d) Fe, and (e) Local conversion degree at 500 sec.

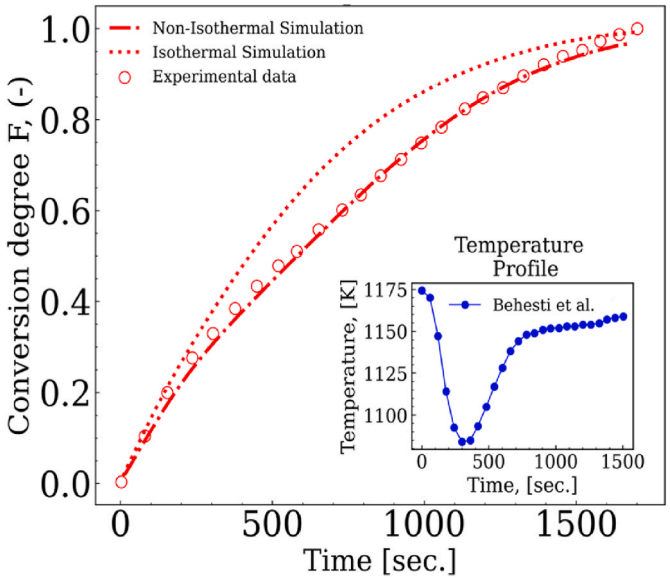

Fig. 14. Fixed bed iron ore pellet conversion degree against reduction time. The experimental data (o-symbols) and temperature profile (subplot) are adopted from Beheshti et al. [14].

temperature distribution for capturing these non-isothermal effects in the reactor. However, addressing the variation of local reduction degree properly requires both spatial and temporal solutions of energy equations in the solid and gas phases. Future work will solve this issue by incorporating a comprehensive energy equation to provide both spatial and temporal temperature distributions within the fixed bed.

4. Conclusion

Modeling the direct reduction process is a challenging task, requiring a reliable kinetic mechanism and a realistic bed structure to obtain accurate results. In this study, a three-step methodology has been presented and validated for particle-resolved CFD simulations of hydrogen-based direct reduction in a fixed bed. Quickly summarized, the three points are: determining kinetic data for single pellets, running a DEM simulation to provide the bed geometry and performing the reactive CFD simulation. The validation has been achieved upon four single pellet experiments, the successful transition from a 1D to a 3D model, the radial bed porosity, and a 500 g iron ore fixed bed experiment. In a second publication [43], we will further show that utilizing spherical particles in the DEM simulation is an acceptable assumption by comparing with a bed of non-spherical particles generated from a CT-scan.

This novel particle-resolved CFD approach gives many insights into the reduction process in fixed beds as the gas phase and pellet state are temporally and spatially resolved. Two major observations were made: first, the large and non-uniform presence of water in the reactor and secondly, the large deviations from the set temperature, which strongly contrast with the ideal single pellet tests where hydrogen concentrations remain high and isothermal conditions are usually assumed. These effects are presumably highly amplified when going further in industrial-scale reactors with a throughput that can reach a hundred tons per hour. For this reason, the model development on single pellets is not sufficient for trustworthy calculations at large scales. Validation at intermediate

scales appears essential. Having a systematic methodology is also crucial as no kinetic model for single pellet reduction is widely accepted. The literature on the topic is abundant, but progress is necessary to capture the intrinsic complexity of this gas-solid reactive system. To the authors' knowledge, no model has for example demonstrated its ability to correctly account for the pellet characteristics, such as size, shape, composition, or porosity, and at the same time its thermodynamic consistency.

Nomenclature

Symbol	Definition	Unit	Symbol	Definition	Unit
λ	Tube to particle ratio	–	$\mathbf{j}_{gi}^{eff}$	Effective diffusive flux	–
D	Bulk diffusion coefficient	$m^2\ s^{-1}$	$M_{i/j}$	Molecular weight	$kg\ mol^{-1}$
d_p	Pellet diameter	mm	$\dot{\omega}_{i/j}$	Chemical source term	$mol\ m^{-3}\ s^{-1}$
m_i	Pellet mass	g	X_j	Mole fraction of species j	–
$\mathbf{v}_i$	Pellet velocity	$m\ s^{-1}$	ε	Porosity	–
$\mathbf{F}_g$	Gravitational force	$kg\ m\ s^{-2}$	$\mathbf{D}$	Constant coefficient	–
$\mathbf{F}_c$	Contact forces	$kg\ m\ s^{-2}$	μ_g	Dynamic viscosity of gas	$kg\ m^{-1}\ s^{-1}$
α_g	Gas volume fraction	–	m_0	Initial pellet mass	g
ρ_g	Density of gas species	$kg\ m^{-3}$	m_∞	Theoretical mass after complete reduction	g
$\mathbf{v}_g$	Gas velocity	$m\ s^{-1}$	F	Global conversion degree	–
S_g	Net mass transfer between phases	–	V_v	Void volume	m^3
$\bar{\bar{\tau}}$	Viscous stress tensor	–	V_T	Total volume	m^3
$\mathbf{g}$	Gravity vector	$m\ s^{-2}$	A_{solid}	Area of the pellet's cross-section in a specific plane	m^2
$\mathbf{M}_{sg}$	Momentum sink term	–	A_{total}	Total area of that specific plane	m^2
ρ_j	Density of solid species j	$kg\ m^{-3}$	r	Radial distance of the plane from bed center	mm
p	Pressure	Pa	h_{plane}	Height of the concentric plane	mm
Y_{gi}	Local mass fraction of gas species	–	C_i	Gas concentration	$mol\ m^{-3}$
D^{eff}	Effective diffusivity	$m^2\ s^{-1}$			

CRediT authorship contribution statement

Mohammed Liaket Ali: Writing – review & editing, Writing – original draft, Visualization, Validation, Software, Methodology, Formal analysis, Data curation, Conceptualization. **Quentin Fradet:** Writing – review & editing, Writing – original draft, Validation, Supervision, Resources, Methodology, Conceptualization. **Uwe Riedel:** Writing – review & editing, Supervision, Project administration.

Declaration of competing interest

The authors declare that they have no known competing financial interests or personal relationships that could have appeared to influence the work reported in this paper.

Appendix A. Supplementary data

Supplementary data to this article can be found online at https://doi.org/10.1016/j.ijhydene.2024.09.028.

References

[1] International Energy Agency Germany. Energy policy review. Paris; 2020. 2020.
[2] Worldsteel Association. 2023 world steel in figures. Brussels 2023.
[3] Joint Research Centre. EU climate targets: how to decarbonise the steel industry. Brussels 2022.
[4] Wei G, Zhu R, Wu X, Dong K, Yang L, Liu R. Technological innovations of carbon dioxide injection in EAF-LF steelmaking. J Occup Med 2018;70(6):969–76. https://doi.org/10.1007/s11837-018-2814-3.
[5] Technologies Midrex. Inc. Direct from midrex: 1st quarter 2020. Charlotte. 2020.
[6] Metolina P, Da Nunis Silva AL, Dixon AG, Guardani R. Multiscale modeling of non-catalytic gas-solid reactions applied to the hydrogen direct reduction of iron ore in moving-bed reactor. Int J Hydrogen Energy 2024;62:1214–30. https://doi.org/10.1016/j.ijhydene.2024.03.151.
[7] Alamsari B, Torii S, Trianto A, Bindar Y. Study of the effect of reduced iron temperature rising on total carbon formation in iron reactor isobaric and cooling zone. Adv Mech Eng 2010;192430:2. https://doi.org/10.1155/2010/192430.
[8] Alamsari B, Torii S, Trianto A, Bindar Y Heat, Transfer Mass. In reduction zone of sponge iron reactor. ISRN Mechanical Engineering 2011;2011:1–12. https://doi.org/10.5402/2011/324659.
[9] Nouri S, Ale Ebrahim H, Jamshidi E. Simulation of direct reduction reactor by the grain model. Chem Eng J 2011;166(2):704–9. https://doi.org/10.1016/j.cej.2010.11.025.
[10] Shams A, Moazeni F. Modeling and simulation of the MIDREX shaft furnace: reduction, transition and cooling zones. J Occup Med 2015;67(11):2681–9. https://doi.org/10.1007/s11837-015-1588-0.
[11] Valipour MS, Saboohi Y. Modeling of multiple noncatalytic gas–solid reactions in a moving bed of porous pellets based on finite volume method. Heat Mass Tran 2007;43(9):881–94. https://doi.org/10.1007/s00231-006-0154-2.
[12] Hamadeh H, Mirgaux O, Patisson F. Detailed modeling of the direct reduction of iron ore in a shaft furnace. Materials 2018;1865(10):11. https://doi.org/10.3390/ma11101865.
[13] Yagi J, Takahashi R, Omori Y. Study on the reduction process of iron oxide pellets in isothermal fixed bed. Tetsu-To-Hagane 1971;57(9):1453–60. https://doi.org/10.2355/tetsutohagane1955.57.9_1453.
[14] Beheshti R, Moosberg-Bustnes J, Kennedy MW, Aune RE. Reduction kinetics of commercial haematite pellet in a fixed bed at 1123–1273 K. Ironmak Steelmak 2016;43(5):394–402. https://doi.org/10.1080/03019233.2015.1104072.
[15] Aguilar J, Fuentes R, Viramontes R. Simulation of iron ore reduction in a fixed bed. Modelling Simul. Mater Sci Eng 1995;3(2):131–47. https://doi.org/10.1088/0965-0393/3/2/001.
[16] Ma K, Deng J, Wang G, Zhou Q, Xu J. Utilization and impacts of hydrogen in the ironmaking processes: a review from lab-scale basics to industrial practices. Int J Hydrogen Energy 2021;46(52):26646–64.
[17] Neumann J, Fradet Q, Scholtissek A, Dammel F, Riedel U, Dreizler A, et al. Thermodynamic assessment of an iron-based circular energy economy for carbon-free power supply. Appl Energy 2024;123476:368. https://doi.org/10.1016/j.apenergy.2024.123476.
[18] Patisson F, Mirgaux O. Hydrogen ironmaking: how it works. Metals 2020;922(7):10. https://doi.org/10.3390/met10070922.
[19] Ranade VV. Computational flow modeling for chemical reactor engineering. first ed. Pune: Elsevier; 2002.
[20] Ma Y, Souza Filho IR, Bai Y, Schenk J, Patisson F, Beck A, et al. Hierarchical nature of hydrogen-based direct reduction of iron oxides. Scripta Mater 2022;114571:213. https://doi.org/10.1016/j.scriptamat.2022.114571.
[21] Valipour MS, Motamed Hashemi MY, Saboohi Y. Mathematical modeling of the reaction in an iron ore pellet using a mixture of hydrogen, water vapor, carbon monoxide and carbon dioxide: an isothermal study. Adv Powder Technol 2006;17(3):277–95. https://doi.org/10.1163/156855206777213375.
[22] Kazemi M, Pour MS, Sichen D. Experimental and modeling study on reduction of hematite pellets by hydrogen gas. Metall Mater Trans B 2017;48(2):1114–22. https://doi.org/10.1007/s11663-016-0895-3.
[23] Ariyan ZG, Mohammad Sadegh V, Mojtaba B. Numerical analysis of complicated heat and mass transfer inside a wustite pellet during reducing to sponge iron by H2 and CO gaseous mixture. J. Iron Steel Res. Int 2016;23(11):1142–50. https://doi.org/10.1016/S1006-706X(16)30169-8.
[24] Zuo H, Wang C, Dong J, Jiao K, Xu R. Reduction kinetics of iron oxide pellets with H2 and CO mixtures. Int J Miner Metall Mater 2015;22(7):688–96. https://doi.org/10.1007/s12613-015-1123-x.
[25] Dutta SK, Sah R. Direct reduced iron: production. In: Colás R, Totten GE, editors. Encyclopedia of iron, steel, and their alloys. CRC Press; 2016. p. 1082–108.
[26] Nyankson E, Kolbeinsen L. Kinetics of direct iron ore reduction with CO-H2 gas mixtures. Int J Eng Res Technol 2015;4(4). https://doi.org/10.17577/IJERTV4IS040955.
[27] Spreitzer D, Schenk J. Reduction of iron oxides with hydrogen—a review. steel research int 2019;1900108(10):90. https://doi.org/10.1002/srin.201900108.

[28] Dong Y. Modeling chemistry and flow in catalytic fixed-bed reactors with detailed geometry: modeling chemistry and flow in catalytic fixed-bed reactors with detailed geometry: TUHH Universitätsbibliothek. 2018.
[29] Jurtz N, Kraume M, Wehinger GD. Advances in fixed-bed reactor modeling using particle-resolved computational fluid dynamics (CFD). Rev Chem Eng 2019;35(2):139–90. https://doi.org/10.1515/revce-2017-0059.
[30] Kinaci ME, Lichtenegger T, Schneiderbauer S. A CFD-DEM model for the simulation of direct reduction of iron-ore in fluidized beds. Chem Eng Sci 2020;115858:227. https://doi.org/10.1016/j.ces.2020.115858.
[31] Zhu HP, Zhou ZY, Yang RY, Yu AB. Discrete particle simulation of particulate systems: a review of major applications and findings. Chem Eng Sci 2008;63(23):5728–70. https://doi.org/10.1016/j.ces.2008.08.006.
[32] Goniva C, Kloss C, Deen NG, Kuipers JA, Pirker S. Influence of rolling friction on single spout fluidized bed simulation. Particuology 2012;10(5):582–91. https://doi.org/10.1016/j.partic.2012.05.002.
[33] Lan B, Xu J, Lu S, Liu Y, Xu F, Zhao B, et al. Direct reduction of iron-ore with hydrogen in fluidized beds: a coarse-grained CFD-DEM-IBM study. Powder Technol 2024;119624:438. https://doi.org/10.1016/j.powtec.2024.119624.
[34] Klerk A de. Voidage variation in packed beds at small column to particle diameter ratio. AIChE J 2003;49(8):2022–9. https://doi.org/10.1002/aic.690490812.
[35] Fradet Q, Ali ML, Riedel U. Development of a porous solid model for the direct reduction of iron ore pellets. Steel Res Int 2022;2200042(12):93. https://doi.org/10.1002/srin.202200042.
[36] Cavaliere P, Dijon L, Laska A, Koszelow D. Hydrogen direct reduction and reoxidation behaviour of high-grade pellets. Int J Hydrogen Energy 2024;49:1235–54. https://doi.org/10.1016/j.ijhydene.2023.08.254.
[37] Sadeghi B, Cavaliere P, Bayat M, Ebrahimzadeh Esfahani N, Laska A, Koszelow D. Experimental study and numerical simulation on porosity dependent direct reducibility of high-grade iron oxide pellets in hydrogen. Int J Hydrogen Energy 2024;69:586–607. https://doi.org/10.1016/j.ijhydene.2024.05.050.
[38] Boccardo G, Marchisio DL, Sethi R. Microscale simulation of particle deposition in porous media. J Colloid Interface Sci 2014;417:227–37. https://doi.org/10.1016/j.jcis.2013.11.007.
[39] Mutailipu M, Liu Y, Chen LY, Song YC. Pore network simulation of two phase flow based on X-ray micro computed tomography images. AMR (Adv Magn Reson) 2014;960–961:254–7. https://doi.org/10.4028/www.scientific.net/AMR.960-961.254.
[40] Akolkar A, Petrasch J. Tomography-based characterization and optimization of fluid flow through porous media. Transport Porous Media 2012;95(3):535–50. https://doi.org/10.1007/s11242-012-0060-7.
[41] Cundall PA, Strack ODL. A discrete numerical model for granular assemblies. Geotechnique 1979;29(1):47–65. https://doi.org/10.1680/geot.1979.29.1.47.
[42] Geuzaine C, Remacle J-F. Gmsh: a 3-D finite element mesh generator with built-in pre- and post-processing facilities. Numerical Meth Engineering 2009;79(11):1309–31. https://doi.org/10.1002/nme.2579.
[43] Ali M.L., Mehlhose S., Fradet Q., Riedel U. Particle-resolved computational modeling of hydrogen-based direct reduction of iron ore pellets in a fixed bed. Part II: Influence of the pellet sizes and shapes. Int J Hydrogen Energy 2024 (Accepted).
[44] Ali ML, Fradet Q, Riedel U. Kinetic mechanism development for the direct reduction of single hematite pellets in H2/CO atmospheres. Steel Res Int 2022;2200043(12):93. https://doi.org/10.1002/srin.202200043.
[45] Kazemi M, Glaser B, Sichen D. Study on direct reduction of hematite pellets using a new TG setup. steel research int 2014;85(4):718–28. https://doi.org/10.1002/srin.201300197.
[46] OpenFOAM. Version 7. The OpenFOAM Foundation. Available from:. 2024. https://openfoam.org/. Accessed May 28, 2024.
[47] Tsuji Y, Tanaka T, Ishida T. Lagrangian numerical simulation of plug flow of cohesionless particles in a horizontal pipe. Powder Technol 1992;71(3):239–50. https://doi.org/10.1016/0032-5910(92)88030-L.
[48] Bai H, Theuerkauf J, Gillis PA, Witt PM. A coupled DEM and CFD simulation of flow field and pressure drop in fixed bed reactor with randomly packed catalyst particles. Ind. Eng. Chem. Res. 2009;48(8):4060–74. https://doi.org/10.1021/ie801548h.
[49] Nijemeisland M, Dixon AG. CFD study of fluid flow and wall heat transfer in a fixed bed of spheres. AIChE J 2004;50(5):906–21. https://doi.org/10.1002/aic.10089.
[50] Muller M, El-Rabii H, Fabbro R. Liquid phase combustion of iron in an oxygen atmosphere. J Mater Sci 2015;50(9):3337–50. https://doi.org/10.1007/s10853-015-8872-9.
[51] Foumeny EA, Moallemi HA, Mcgreavy C, Castro JAA. Elucidation of mean voidage in packed beds. Can J Chem Eng 1991;69(4):1010–5. https://doi.org/10.1002/cjce.5450690425.
[52] Dixon AG. Correlations for wall and particle shape effects on fixed bed bulk voidage. Can J Chem Eng 1988;66(5):705–8. https://doi.org/10.1002/cjce.5450660501.
[53] Benyahia F, O'Neill KE. Enhanced voidage correlations for packed beds of various particle shapes and sizes. Part Sci Technol 2005;23(2):169–77. https://doi.org/10.1080/02726350590922242.
[54] Fradet Q, Kurnatowska M, Riedel U. Thermochemical reduction of iron oxide powders with hydrogen: review of selected thermal analysis studies. Thermochim Acta 2023;179552:726. https://doi.org/10.1016/j.tca.2023.179552.
[55] Heidari A, Niknahad N, Iljana M, Fabritius T. A review on the kinetics of iron ore reduction by hydrogen. Materials 2021;14(24). https://doi.org/10.3390/ma14247540.